SANDIA REPORT

SAND96–1794 • UC–704
Unlimited Release
Printed July 1996

A Novel Method to Characterize the Elastic/Plastic Deformation Response of Thin Films

Roy J. Bourcier, Jeff J. Sniegowski, Vicki L. Porter

Prepared by
Sandia National Laboratories
Albuquerque, New Mexico 87185 and Livermore, California 94550
for the United States Department of Energy
under Contract DE-AC04-94AL85000

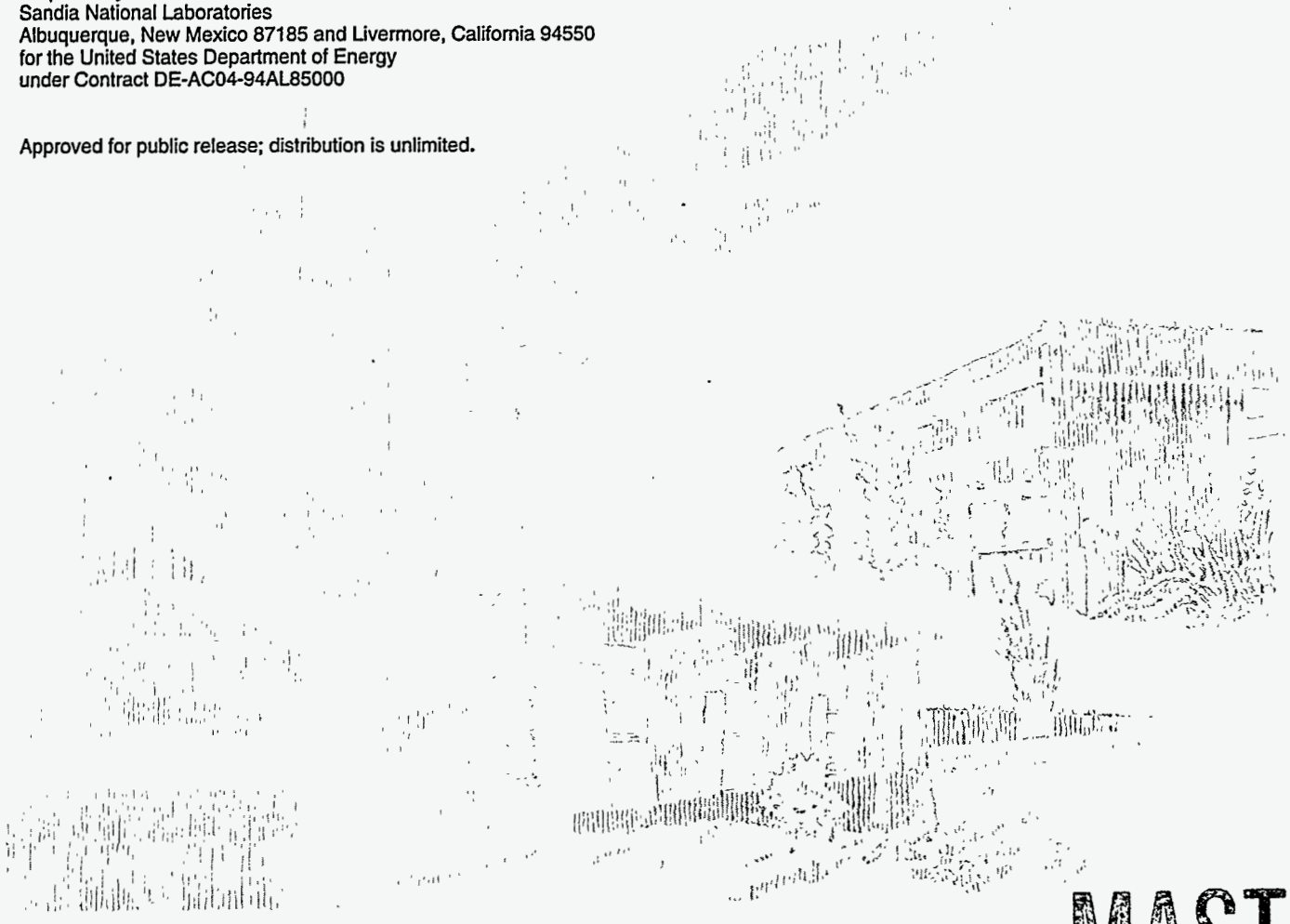

Issued by Sandia National Laboratories, operated for the United States Department of Energy by Sandia Corporation.

Available to DOE and DOE contractors from
Office of Scientific and Technical Information
PO Box 62
Oak Ridge, TN 37831

Prices available from (615) 576-8401, FTS 626-8401

Available to the public from
National Technical Information Service
US Department of Commerce
5285 Port Royal Rd
Springfield, VA 22161

NTIS price codes
Printed copy: A03
Microfiche copy: A01

DISCLAIMER

SAND96-1794
Unlimited Release
Printed July, 1996

Distribution Category UC-704

A Novel Method to Characterize the Elastic/Plastic Deformation Response of Thin Films

Roy J. Bourcier
Mechanical and Corrosion Metallurgy Department

Jeff J. Sniegowski
Integrated Micromechanics, Microsensors and CMOS Technology Department

Vicki L. Porter
Material and Structural Mechanics Department

Sandia National Laboratories
Albuquerque, NM 87185

Abstract

A novel experimental/numerical test method has been developed which allows accurate characterization of the elastic and large-strain plastic mechanical response of thin films. Silicon micromachining techniques have been used to fabricate isolated film features which are mechanically tested using our ultralow-load indentation test system. Macro-scale laboratory testing and finite element analysis were employed to optimize the design of the geometric feature used and to benchmark our analysis capabilities. A simple rigid-plastic geometric analysis of our test structure is developed and applied to the observed force-displacement response, allowing us to extract the uniaxial inelastic stress-strain response of micrometer-scale thin film structures. To our knowledge, this is the first time that the inelastic deformation behavior of metal alloy features of this size scale has been quantitatively determined.

Introduction

The mechanical properties of thin films are of significant technological interest. Their effective use in technologies such as integrated circuits, magnetic storage, reflective coatings and micromachine technology would be greatly enhanced by a thorough knowledge of their mechanical properties. Unfortunately, the measurement of such properties is a vexing experimental problem. A large number of experimental methods have been developed and applied in an attempt to facilitate such measurements. A brief review of this technology is helpful in understanding the need for continued work (more thorough reviews are available for those who are interested [1,2]).

Test techniques to characterize the mechanical properties of thin films can essentially be divided into two groups: liberated and insitu testing. Liberated films are generally subjected to miniaturized versions of conventional macroscale test methods such as uniaxial tensile testing [3-9] or bulge testing [10-14]. Such techniques are fraught with difficulty. Once removed from their underlying substrate, thin films are very delicate and easily damaged. Also, test specimens prepared from liberated thin films generally have very severe aspect ratios (ie, small in one dimension - film thickness) relative to the conventional macroscale test specimens which they attempt to mimic. This leads to a tendency to mechanical instability during testing, resulting in a plastic deformation response dominated by geometric and microstructural heterogeneities rather than the intrinsic flow behavior of the film itself.

In part to avoid these difficulties, films are often characterized insitu, generally through the use of nanoindentation testing [15-21]. The fundamental advantages of this technique are the inherent damage resistance during handling of a film which remains attached to its substrate and the ability to sample extremely small volumes of material. Significant work has been performed in recent years to enhance our understanding of the nanoindentation behavior of thin films and near-surface layers [22-27]. Nonetheless, significant complications still exist. For sufficiently thin films (or sufficiently deep indentations) the substrate makes a significant (and poorly characterized) contribution to the load-depth indentation response. The influence of indenter/sample friction on the load-depth response is difficult to know apriori and difficult to even characterize. The indentation strain field is complex and does not correlate well to a conventional uniaxial stress strain curve, the most commonly measured engineering deformation response. The indentation method at best (assuming the above difficulties are overcome) measures some average value of 'flow stress' - it shows extremely poor ability to resolve the complex interaction between yield strength and strain hardening behavior in a material.

In recent years, nanoindentation has been used to probe the mechanical response of simple micromachined cantilever beams [28-31]. This methodology allows both accurate determination of the elastic modulus (in bending) and approximate determination of the yield strength of insitu thin films. Unfortunately, simple, 'diving board'-type cantilever beams do not allow the determination of the large strain plastic deformation response of films - at best they can be used to obtain a reasonable indication of yield strength. Also, their high mechanical compliance makes it necessary to make them larger than may be desired to allow the nanoindentation test system to detect contact.

In an attempt to address most if not all of the above difficulties, we have developed a unique experimental method for the determination of the 'insitu' uniaxial inelastic stress-strain response of metallic thin films. Photolithographic micromachining techniques have been used to fabricate micromechanical test structures designed with the assistance of large strain inelastic finite element modeling. The structures used are straight beams (rigidly fixed at both ends) of complex cross section (fully contained within a 1x6x20 μm volume) which span a deep cavity in an underlying silicon wafer. A wedge shaped diamond indentation probe is used to deform the structures into the cavity, causing the development of three plastic hinges followed shortly by the tensile deformation of ligaments (each 6μm long x 3μm wide x 1 μm thick) on either side of the indentation probe. A

simple rigid-plastic geometric analysis of our test structure is used to interpret the force-displacement response, allowing us to extract the uniaxial inelastic stress-strain response of micrometer-scale thin film structures.

Procedure

Test Feature Design

The basic test specimen geometry explored in this study is shown schematically in Figure 1. This test feature can be characterized as a constant thickness beam of variable width fixed at both ends. The wide section in the center of the beam serves as the contact pad for a wedge-shaped mechanical probe, as shown. Our goals during the development of this design were the following:

1) The specimen must be fabricable using conventional micromachining technology.

2) Desired levels of specimen deformation must occur at loads and displacements which are within the limits of detection of our NanoIndenter®.

3) The plastic deformation response of the specimen should be largely dominated by tensile deformation.

4) The specimen should allow detection of near yield deformation, large strain plastic flow, and tensile rupture.

5) The specimen should show good discrimination in the force-displacement response between materials of differing mechanical response (yield strength, strain hardening, ductility).

Continuum-Scale Mechanical Testing

In order to accelerate the successful design of our micromechanical test feature and to provide a benchmarking target for our finite element simulations, continuum-scale mechanical testing was performed. A fixture, shown in Figure 2, was designed to allow punch testing on a conventional servohydraulic mechanical test frame of beam specimens of a wide range of lengths and profile. Specimens tested were 0.635 cm = 1 μm scale versions of the micromechanical test feature machined from 1100 aluminum alloy plate and subsequently annealed to the T0 condition. Uniaxial tensile tests were performed on conventional plate specimens fabricated from the same material to determine large-strain plastic constitutive parameters for use in finite element simulations of the punch tests.

Finite Element Modeling

Large strain quasistatic finite element analysis was performed to guide the development of our test feature. A finite element model of the continuum-scale specimen is shown in Figure 3. Due to symmetry, only one-quarter of the beam is modeled. The analysis was performed using JAS3D, a finite element code for quasi-static structural analysis currently under development at Sandia. For this problem, it was found that the dynamic relaxation solution algorithm was the most suitable. In order to facilitate convergence, the punch was held fixed and an upward displacement applied to the fixed end of the beam. The total reaction force is then obtained as the sum of all the reaction forces at the nodes on the surface of the punch.

Photolithographic Micromachining of Microscale Test Features.

Once a basic specimen design was adopted, the series of processing steps necessary to fabricate test structures was developed. The fabrication technology used to produce the micromechanical test features combines two MicroElectroMechanical Systems (MEMS) fabrication technologies. Surface micromachining techniques in film deposition, patterning, and etch definition are used to produce the test features themselves, for example, the doubly clamped beams of aluminum metal,

while bulk silicon micromachining is used to produce the sufficiently deep well beneath the test structures. The typical result is a structure, such as the doubly-clamped beam suspended above a well on a silicon wafer substrate, shown in Figure 4.

Both MEMS technologies are heavily based on the common fabrication methods found in silicon Integrated Circuit process facilities. In our case, Sandia's Microelectronics Development Laboratory facility was used. However, for this specific application, the particular combination of materials and micromachining techniques required considerable effort to develop. Particular care must be taken, in the case of an electronics foundry, to not introduce cross-contamination in the electronics fabrication area. The basic process flow developed addresses the issues of decontamination which allows reproduction of these material specimens in an IC-type fabrication house.
In these experiments, the process makes use of 6 inch (110) oriented single-crystal silicon substrates. The photolithographic patterning capability provides resolution capability below 1 micrometer . The required thin film deposition capabilities exist in-house. The technology development consisted of first, combining the basic feature geometry with the crystal orientation of the substrates and second, tailoring the existing in-house thin films with selective dry and wet chemical etch processes. Details of these issues are discussed below.

Issues

Two primary issues existed in the fabrication of the test features. The first was determination of a method to produce an adequately deep well under the structures to allow sufficient deformation of the test structure below the plane of the wafer which provides the desired behavior in the test specimen. Simple surface micromachining techniques [33] can readily be used to produce doubly-clamped suspended beams for example, but the separation to the underlying substrate is typically on the same order as the thickness of the feature structure thickness. This is inadequate to allow large-deflection deformation in the test specimen. Therefore, the technique of using anisotropic silicon etchants to cut deep wells under the structures was adopted, that is, a bulk silicon micromachining technique[34]. Although this technique has been used to produce cantilevered beams, the technique applied on (100) oriented silicon substrates does not readily produce doubly-clamped suspended beams with well-defined, orthogonal boundary conditions. The solution was to use another, the (110), orientation of silicon substrates. The details are discussed in the section on (110) silicon.

The second primary issue was to develop or modify dry and wet chemistries to selectively etch the thin-films which comprise the test structures themselves without significantly etching into the supporting silicon substrate nor compromise the mechanical integrity of the beams. An overetch into the silicon substrate has the effect of causing an undercut of the protected areas which moves the boundary conditions of the structure. The wet chemistries used to etch the well in the silicon must be selective to the beam material so not to compromise its material integrity. In the case of silicon nitride and tungsten beams, potassium hydroxide (KOH) is highly selective. In fact, silicon nitride is the preferred mask material for KOH when defining areas to be etched in the silicon. In the case of aluminum, a suitably selective etchant was found with some guidance from the literature [35]. These chemistries are discussed in the section on bulk etching.

(110) Silicon

Usually bulk micromachining of silicon refers to a class of crystal-plane selective etchants. These etchants normally etch all planes of silicon faster than the (111) close-pack family of planes in silicon. Therefore, the terminal structures defined in bulk micromachining have (111) surfaces. For example, a square opening defined on a (100) silicon wafer when anisotropically etched produces a pyramidal pit with (111) side-walls sloped at 54.7° to the surface. Such a pit would be adequate for

a bridge suspended over it, except that when a beam is oriented along a direction which produces a (111) plane it will not be undercut to form such a well. This can be circumvented if the beam is laid out along a diagonal of the rectangular well area. In this orientation, the beam will be undercut and it will span a pyramidal pit across its diagonal. This however, produces a non-orthogonal boundary condition at the ends of the beam.

To overcome this limitation, one can use (110) oriented silicon, i.e. silicon wafers with a (110) plane for its surface. Specifically, the wafers used were 20 Ω-cm, n-type dopant (phosphorus-doped) silicon with (110) surface and with a wafer flat in the <111> direction. Such a wafer produces a pit as shown in Figures 5 and 6. Figure 5 depicts a plan-view of a pit area with a beam suspended across it. The dotted blue lines indicate conjunction of (111) etched surfaces. Figure 6 illustrates two major cross-sections through a well area. In particular, note that the ends of the beam are attached orthogonally to the substrate and that the substrate slopes downward away for the beam end at 35 °. Also note that at the top and bottom edges (horizontal edges) defined by the mask are undercut. This behavior to undercut mask edges in this direction allows the undercut of the beam so that it is suspended over the pit. Note that in the vertical direction, the mask is not undercut and so a well-defined boundary is formed at the ends of the beam.

Thin Film Etching

In these experiments, three thin films were investigated: a Low-Pressure-Chemical-Vapor-Deposited (LPCVD) silicon-rich, low-stress silicon nitride film commonly used in MEMS technology, a LPCVD tungsten film commonly used in the IC industry, and an sputtered aluminum film also commonly used in the IC industry.
The basic process used to define the beam and pit pattern in the desired thin films was Reactive Ion Etching (RIE). RIE is referred to a "dry" etch process since it is based on the use of gases and plasmas. It is necessary due to the fine geometry and desired tolerances of the beam structures. The RIE processes used here were highly anisotropic, typically producing sidewall slopes at or greater than 88° to the substrate plane. This allows retention of the rectangular cross-section to the beams.

Each thin film requires specific RIE chemistry to etch them. Most of which are common to IC-processing. A requirement of the RIE etch was that it does not substantially etch into the silicon once it etches through the thin film. If etch into the silicon occurs, it moves the attachment point of the beam to the silicon away from the end of the beam effectively making the beam longer. This occurs due to the mask being undercut at the end of the beam.
In the case of the aluminum thin film, a thin layer of silicon dioxide was deposited before the aluminum (a couple hundred angstroms of oxide are adequate). This thin oxide layer serves as an etch-stop for the RIE once it punches through the aluminum. This oxide can then be removed by a buffered oxide etchant which consists of ammonium fluoride:hydrofluoric acid:ethylene glycol in the ratio 8:1:1. This etchant does not significantly attack the aluminum before it removes the oxide layer.

Bulk Etching

Silicon nitride and Tungsten: For these two films, potassium hydroxide works very well as the bulk silicon etchant. Neither film is etched significantly during the well formation. That is, while the silicon is etching at a rate of approximately 0.5 micron/minute, these films are etched at a rate of a few angstroms/minute. The exact KOH recipe used is not critical. In these experiments, 6 molar and 8 molar solutions of KOH at 85°C were used with identical results.

Aluminum: Aluminum posed the greatest difficulty. KOH attacks aluminum aggressively. The literature indicated that a Tetramethyl Ammonium Hydroxide (TMAH) and water solution, if properly preloaded with silicon, becomes selective to aluminum while etching silicon

anisotropically. After experimentation, it was found that a 25 wt.% solution of TMAH loaded with approximately 100g/l silicon at 83°C for 10 minutes works well. Figures 7a and b are SEM micrographs of an aluminum beam produced by this process.

Micromechanical Testing

All testing was performed using a NanoIndenter® micromechanical test system with a custom diamond probe. The probe used is a wedge whose apex is approximately 8 μm long with a 0.1μm radius of curvature with an included angle between the major faces of roughly 70°.

Results and Discussion

Continuum-scale Mechanical Testing

Engineering stress-strain curves obtained from uniaxial tensile testing of the 1100-0 aluminum plate used in this study is shown in Figure 8. These results are highly reproducible and typical of this alloy in the specified condition. These test results were used to obtain the parameters for the best fit of a hardening model. In this case, the theoretical description of hardening follows an inverse hyperbolic sin,

$$\sigma = \sigma_y + A\sinh^{-1}(l\varepsilon)$$

where A and l, as well as the yield stress (σ_y) are material parameters. Values for Young's modulus (E) and Poisson's ratio (ν) were obtained from the literature [32]. The constitutive parameters for this 1100 aluminum material are given in Table 1 below and the fit is shown in Figure 9. As can be seen in the figure, the fit of the theoretical curve and the actual stress-strain data are very close.

The force-displacement response for an 1100-0 continuum scale test article is shown in Figure 10. The curve displays four distinct regios of behavior: 1) a short linear section with an abrupt knee, 2) an extended region of upward concave curvature, 3) an extended region of downward concave curvature and 4) an abrupt downturn terminating in fracture. Fracture unavoidably occurs in only one tensile ligament - however, deformation appears to be equally balanced until very near failure. This is borne out by the fact that the point of contact between the indenter probe and the sample remains fixed throughout the life of the test. If deformation was unbalanced, this point would slide toward one end of the specimen, which is not observed.

Finite Element Modeling of Test Feature

A quantitative comparison of the finite element results and the measured force-deflection behavior of the aluminum test specimen is shown in Figure 11. Correlation between the two is good, with the most encouraging aspect being the fact that the slopes are very nearly the same over a large portion of the deformation, even though there is some offset between the curves. The test frame is not completely rigid so the experimental results show more deformation for the same load. It is expected that this difference will be less pronounced in the micromechanical test because the boundary conditions applied to the fixed end of the beam, although reasonable for the scaled-up test, more accurately represent those of the micromechanical film test. In the finite element model, the entire bottom surface of the wide end of the beam is given the same prescribed displacement, and the top surface is free similar to a film attached to a substrate. However, in the scaled-up test, each end of the beam is clamped in place by two bolts.

In addition, the finite element results show a lower maximum load than the test results, although the difference is only 7%. The maximum load occurs at the point where the test piece (or finite

element model) begins to experience highly localized deformation in the ligament. The difference in maximum load and post-peak behavior between the test and the simulation may be due to the fit of the theoretical curve at maximum load in the tensile test. In order to get a better simulation of post-peak behavior, finite element simulation of the tensile tests would be required. However, since the most important aspect in this problem is the strain-hardening behavior and not prediction of failure, it was deemed unnecessary to get a better representation of post-peak behavior.

The computed finite element deformation also compares favorably with the experimental results in several aspects. Figure 12 shows two views of the finite element model immediately following localization. The localization is predicted to occur near the center of the ligament and this was seen in the test specimen in approximately the same location. This is also encouraging for the specimen design because it indicates that the most highly strained region is in the ligament and that the stress is mainly due to uniaxial stretching with negligible bending. That is, it results in a load-controlled failure similar to that in a tensile test. The three-dimensional nature of the localization can be seen in the blow-up with the section narrowing more at the center than the edges. This feature is also apparent in the test specimen.

Another qualitative aspect is the deformation of the widened contact pad beneath the punch. Both the test specimen and the finite element simulation clearly show out-of-plane bending at the center of the beam. As indicated in Figure 13, the outer edge of the contact pad bends downward away from the punch. This aspect could only be modeled correctly by including the punch in the simulation. The computational results were also used to evaluate the design of the test specimen for measuring strain-hardening behavior. For a good design, it is desired to have most of the strain energy concentrated in nearly uniaxial extension of the ligaments throughout a large portion of the deformation history. The amount of strain energy is indicated by the levels of plastic strain in the specimen as well as the volume over which they act. In addition, the uniaxial stretching of the ligament (as opposed to bending) is indicated by the uniformity of plastic strain throughout the ligament, both in the length and across the cross-section. Figures 14 and 15 show computed plastic strain contours over the surface of the test specimen and through the cross-section at the center of the ligament, respectively.

Figure 14 shows that early in the deformation (0.5in deflection), the highest levels of plasticity are concentrated in the upper surface near the end of the beam and in the lower surface at the center. Some plasticity also occurs directly underneath the punch in a small region. At the same time, plastic strain is wide-spread through the ligament albeit at a lower level.

By the time deflection has reached 1.0 in and 1.5 in, the plastic strain is clearly uniform over a large volume of the ligament. Although the level of plastic strain is still higher at the hinges, these values encompass a much smaller volume of material. Therefore, it is clear that by this stage of deformation, most of the strain energy is in the ligament of the specimen.

Finally, the last picture of Figure 14 shows the plastic strain distribution when the vertical deflection has reached 2.0in. At this point the beam is exhibiting necking in the ligament and the plastic strain contours clearly indicate the localization in this region.

Figure 15 shows the plastic strain contours through the cross-section at the center of the ligament for various stages of deformation. The top picture show that there is some variation of plastic strain across the depth of the cross-section at a deflection of 0.5in, but the variation is small compared with the actual level of plastic strain. When the deflection has reached 1.6in, the variation across the depth is insignificant, indicating that the deformation in this section is nearly uniform as desired. At this level, some variation is seen across the width due to the edge effect, but these variations are only 2% of the level of plastic strain. Finally, by the time the specimen has necked at a deflection of 2.0in, the three-dimensional affects on the strain field are clearly visible across the width of the section, but the strain through the depth of the cross-section is still very uniform.

Micromechanical Testing of Microscale Test Features.

The force-displacement response of tungsten and silicon nitride micromechanical test structures is shown in Figure 16. Both materials display nearly fully elastic response up to the point of fracture with no significant mechanical hysteresis. The response of these structures is thus amenable to analysis using simple small strain elastic beam theory. To facilitate this comparison, simplified test articles were fabricated. These were simple straight beams (no end radii, no center contact patch) of rectangular cross section 1x3x20 μm. The elastic mechanical response of this geometry can be analyzed for a central point load using the simple expression:

$$y=-(Wl)/(192EI)$$

where y = deflection
W = applied load
l = length of beam
E = elastic modulus
I = bending moment

The bending moment for a beam of rectangular cross section can be expressed as:

$$I = bd^3/12$$

where b = width of beam section
d = height of beam section

Assuming the published elastic modulus of 50,000,000 psi for polycrystalline tungsten [32], one can obtain good agreement with the experimental force displacement results, as seen in figure 17.

The force - displacement response of aluminum micromechanical test structures is illustrated in Figures 18 and 19. Figure 18 shows results from a series of tests on different test articles at the same loading rate, demonstrating the reproducibility of the observed response. Representative curves from a series of tests performed at different loading rates are shown in Figure 19. These tests exhibit a modest elevation of the load - depth response with increasing deformation rate, which is consistent with the observed trends in conventional continuum - scale mechanical testing of polycrystalline aluminum.

Analysis of the Deformation Response of Continuum-Scale Test Feature

To a first approximation, the plastic deformation response of our test specimen can be modeled as a simple assemblage of rigid and inelastic members connected by pinned joints. The simplest such model is shown in Figure 20. Here, each half (length l_i) of the specimen is treated as a linear series of rigid-inelastic-rigid beams, connected together at the center and mounted at the ends by frictionless pinned joints. A vertical point load P is applied at the central pinned joint and is resolved into its tensile components in the inelastic beam elements (whose width, thickness and length are w, t and g, respectively) . Tensile stress is calculated by assigning to the inelastic beam elements the same cross-sectional area as the tensile ligaments of our test feature. Vertical displacment of the central pinned joint is wholly converted to extension of the inelastic elements. The resulting equations for engineering stress (S) and engineering strain (e) of the inelastic elements as a function of displacement d are:

$$S = P / (wt \cdot \sin(\arctan(d / li)))$$
$$e = ((d / \sin(\arctan(d / li))) - li) / g$$

The results of applying this simple analysis to our continuum-scale test specimen are shown in Figure 21. It can be seen that we are able to predict the engineering stress-strain response of 1100-0 aluminum to within 5% accuracy for any specified strain between 2 and 30%. This suggests that the bulk of the strain energy deposited into the test article is realized as uniaxial deformation of the tensile ligaments for much of the specimen life.

Having gained a significant measure of confidence in this simple analytical model, we now apply it to the analysis of our aluminum micromechanical test structures. Stress-strain curves calculated for three representative aluminum micromechanical tests are shown in Figure 22. The first thing to be noted is that for strains >~2%, the model predicts a relatively flat stress - strain response with a maximum engineering stress of 150-170 MPa. These characteristics are consistent with behavior which might be observed in continuum - scale testing of polycrystalline aluminum. The predicted tensile strength is near the high end of the values which might be expected, a reasonable result given the sub - micron grain size of the sputtered film examined here. The low ductility of these thin film structures (a calculated uniform strain of <10%) is surprising. However, close examination of the aluminum micromechanical test structures reveals that there may be residual thermal oxide bonded to the micromechanical test structure following processing. If present, such an oxide film would fracture at small strains in a brittle manner during indentation testing. This could result in a zone of intense plastic strain localization in the aluminum film, resulting in a ductile shear failure a t a low level of uniform strain in the tensile ligaments. We were unable to refine our processing of the aluminum test structures before the end of this project to test this hypothesis. Also somewhat disconcerting is the seemingly nonphysical behavior predicted by our simple analytical model at small (<2%) strains, with stress rising asymptotically as we approach a zero strain condition. This is mainly due to violation of the underlying assumptions of the basic analytical model: 1) that deformation of the specimen consists solely of uniaxial stretching of the tensile ligaments and 2) that there is no elastic deformation of the structure.

Conclusions

•We have successfully developed a novel experimental/numerical test method which allows accurate characterization of the elastic and large-strain plastic mechanical response of thin films.

•Macro-scale laboratory testing and finite element analysis were employed to optimize the design of the geometric feature used and to benchmark our analysis capabilities.

•Silicon micromachining techniques have been used to fabricate isolated film features which are mechanically tested using an ultralow-load indentation test system.

•A simple rigid-plastic geometric analysis of our test structure is developed and applied to the observed force-displacement response, allowing us to extract the uniaxial inelastic stress-strain response of micrometer-scale thin film structures.

•To our knowledge, this is the first time that the inelastic deformation behavior of metal alloy features of this size scale has been quantitatively determined.

Acknowledgements

The authors wish to thank David T. Schmale for performing all of the mechanical testing reported here. This work was performed at Sandia National Laboratories supported by the U.S. Department of Energy under Contract DE-AC04-94AL85000.

References

[1] D. A. Hardwick, Thin Solid Films 154 (1987) 109-124.
[2] R. J. Bourcier, "Micromechanical Characterization of Near Surface Layers, Proceedings of 1989 Microbeam Analysis Society Meeting.
[3] S. S. Brenner, J. Appl. Phys. 28 (1957) 1023.
[4] C. A. Neugebauer, J. Appl. Phys. 31 (1960) 1096.
[5] D. Kuhlman-Wilsdorf and K. S. Raghavan, Rev. Sci. Instrum. 33 (1962) 930.
[6] A. Lawley and S. Schuster, Rev. Sci. Instrum. 33 (1962) 1178.
[7] J. M. Blakely, J. Appl. Phys. 35 (1964) 1756.
[8] A. Jankowski and T. Tsakalakos, J. Appl. Phys. 57 (1985) 1835.
[9] C. G. Andeen, C. W. Hagerling and R. W. Hoffman, Proc. 7th Int. Vacuum Congr. and 3rd Int. Conf. on Solid Surfaces, Vienna, Austria, 1977, p. 1769.
[10] J. W. Beams, in C. A. Neugebauer, J. D. Newkirk and D. A. Vermilyea (eds.), The Structure and Properties of Thin Films, Wiley, New York, 1959, 183.
[11] W. M. C. Yang, T. Tsakalakos and J. E. Hilliard, J. Appl. Phys. 48 (1977) 876.
[12] T. Tsakalakos, Thin Solid Films 75 (1981) 293.
[13] A. J. Griffin, Jr., F. R. Brotzen and C. F. Dunn, Thin Solid Films 150 (1987) 237.
[14] F. R. Brotzen, C. T. Rosenmayer and R. J. Gale, Thin Solid Films 166 (1988) 291.
[15] J. B. Pethica, in "Ion Implantation Into Metals", (eds. V. Ashworth, W. Grant and R. Proctor), Pergamon Press, Oxford, 1982, p. 147.
[16] J. B. Pethica and W. C. Oliver, in S. T. Picraux and W. J. Choyke (eds.), Metastable Materials Formation by Ion Implantation, Elsevier, Amsterdam, 1982, pp.373-79.
[17] J. B. Pethica, R. Hutchings and W. C. Oliver, Nucl. Instrum. Methods, 209-210 (1983) 995-1000.
[18] W. C. Oliver, R. Hutchings and J. B. Pethica, Metall. Trans. A, 15 (1984) 2221-2229.
[19] M. F. Doerner and W. D. Nix, J. Mater. Res. 1 (1986) 601.
[20] W. C. Oliver, C. J. McHargue and S. J. Zinkle, Thin Solid Films, 153 (1987) 185-196.
[21] W. C. Oliver and C. J. McHargue, Thin Solid Films, 161 (1988) 117-122.
[22] R. Hill, The Mathematical Theory of Plasticity, Clarendon, London, 1950.
[23] P. J. Burnett and D. S. Rickerby, Surface Engineering 3 (1987) 69.
[24] A. Bhattacharya and W. D. Nix, Int. J. Solids Struct., 24 (1988) 881.
[25] A. G. Tangena and G. A. M. Hurkx, J. Eng. Mat. Technol. 108 (1986) 230.
[26] R. J. Bourcier, C. M. Stone, and F. G. Yost, Sandia National Laboratories Report SAND85-0486, September 1985.
[27] R. J. Bourcier, S. M. Myers and D. H. Polonis, Nuclear Instruments and Methods in Physics Research B44 (1990) 278-288.
[28] T. P. Weihs, S. Hong, J. C. Braveman and W. D. Nix, J. Mater. Res. 3 (5), 931-942.
[29] S. Hong, J. C. Braveman, T. P. Weihs and O. K. Kwon, MRS Symp. Proc., vol. 108, 1987.
[30] S. Johansson and J. Å. Schweitz, J. Appl. Phys. 63 (10) 4799-4803.
[31] S. Johansson, F. Ericson and J. Å. Schweitz, J. Appl. Phys. 65 (1) 122-128.
[32] Metals Handbook, ASM International, 1994.
[33] R. T. Howe and R. S. Muller, "Polycrystalline Silicon Micromechanical Beams," J. Electrochem. Soc.:SOLID-STATE SCIENCE AND TECHNOLOGY, Vol. 103, No. 6, pp. 1420-1423, June 1983.
[34] K. Peterson, "Silicon as a Mechanical Material", Proc. IEEE, vol. 70, no. 5, pp. 420-457, May 1982.
[35] U. Schnakenberg, W. Beneke, and P. Lange, "TMAHW Etchants for Silicon Micromachining", Proc. 1991 Intl. Conf. on Solid-State Sensors and Actuators (TRANSDUCERS 91), San Francisco, CA, June 24-27, 1991, pp. 815-818.

Appendix A. Required LDRD Information

Awards:
none

Publications and Presentations:
Publication: "A Novel Method to Characterize the Elastic/Plastic Deformation Response of Thin Films", in preparation.
Presentation: "A Nanoindentation-Based Method to Determine the Tensile Deformation Response of Thin Films", presented at Spring MRS Meeting, San Francisco, CA, April 8-12, 1996.

Patents:
none

Copyrights:
none

Employee Recruitment:
none

Student Involvement:
none

Follow-on Work:
A large ($1.5M) interdisciplinary DOE-BES proposal entitled "A Study of the Limits of High Strain Rate Superplasticity in Aluminum Alloys" has been prepared and submitted following acceptance of the preproposal. We have not yet been notified of status of review. This proposal was based on the experimental capabilities developed in this LDRD project.

Tables

Table 1. Material Parameters

Young's Modulus = 10000 ksi
Poisson's Ratio = 0.30
Yield Stress = 1.91 ksi
A = 3.09 ksi
l = 139

Figures

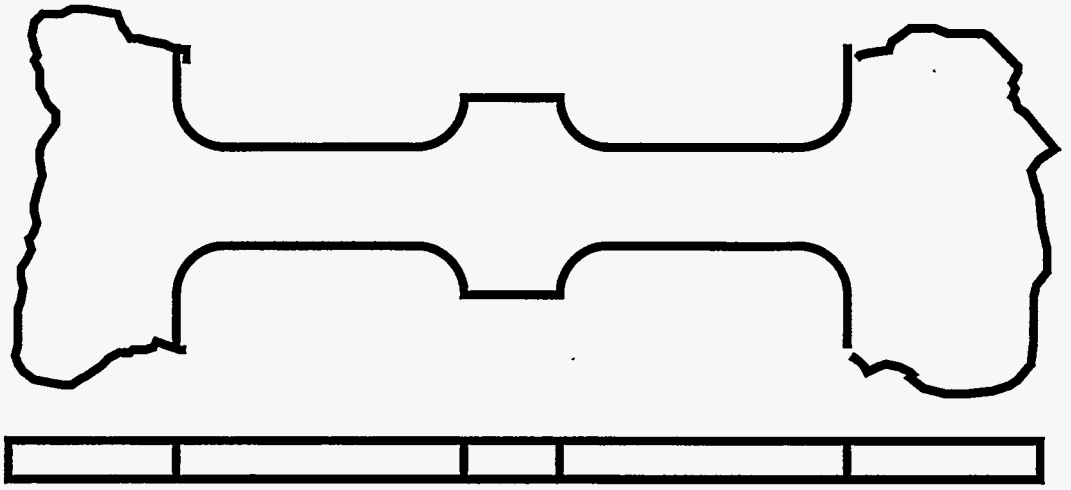

Figure 1. Schematic of the micromechanical test structure developed in this study.

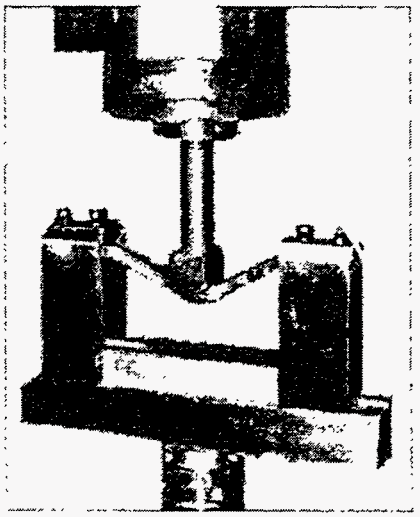

Figure 2. Continuum-scale test system used in design of micromechanical test feature.

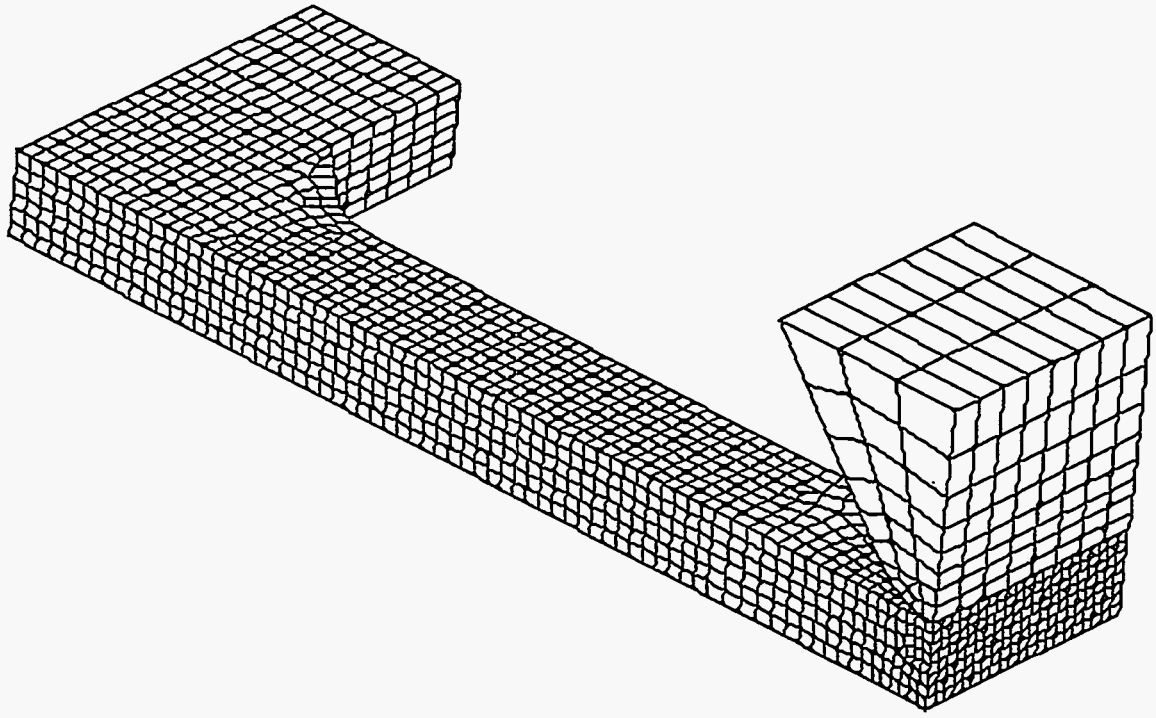

Figure 3. Finite element model of continuum scale test feature and indentation probe.

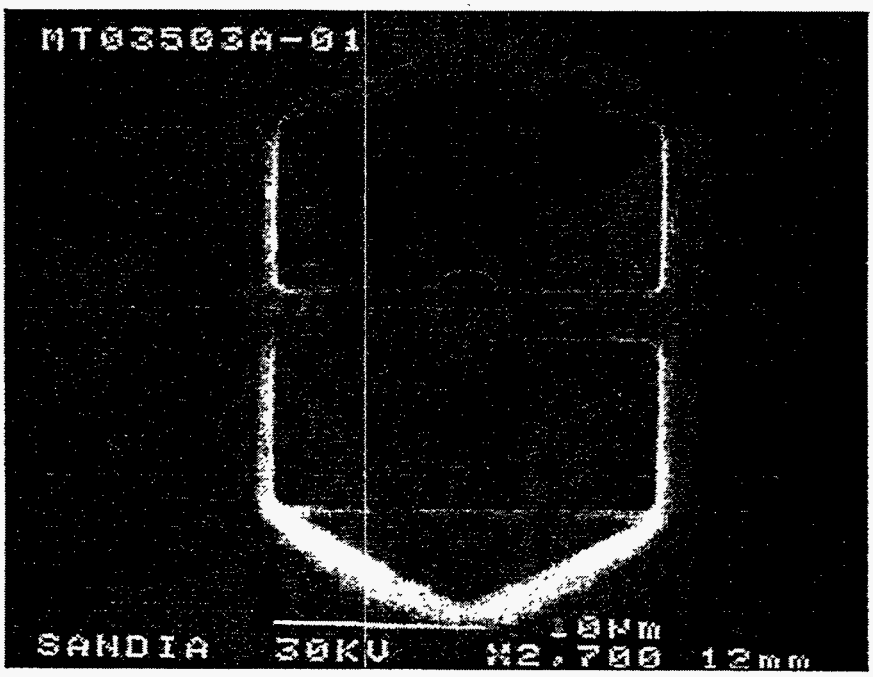

Figure 4. SEM plan-view micrograph of a silicon nitride doubly-clamped beam suspended across a well etched in (110) orientation silicon substrate. Beam geometry is width 3 microns, length 20 microns, thickness 0.8 micron over a well with walls sloped at 35° to the plane of the surface for a mid-depth of 8 microns.

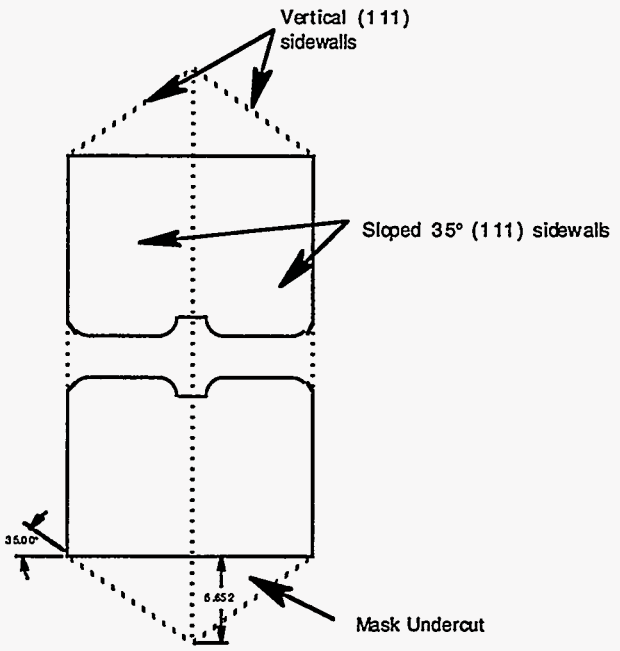

Figure 5. Schematic plan-view of a simple pit with a suspended beam across it. The dotted lines indicate the conjunctions of various planes and thin film surfaces.

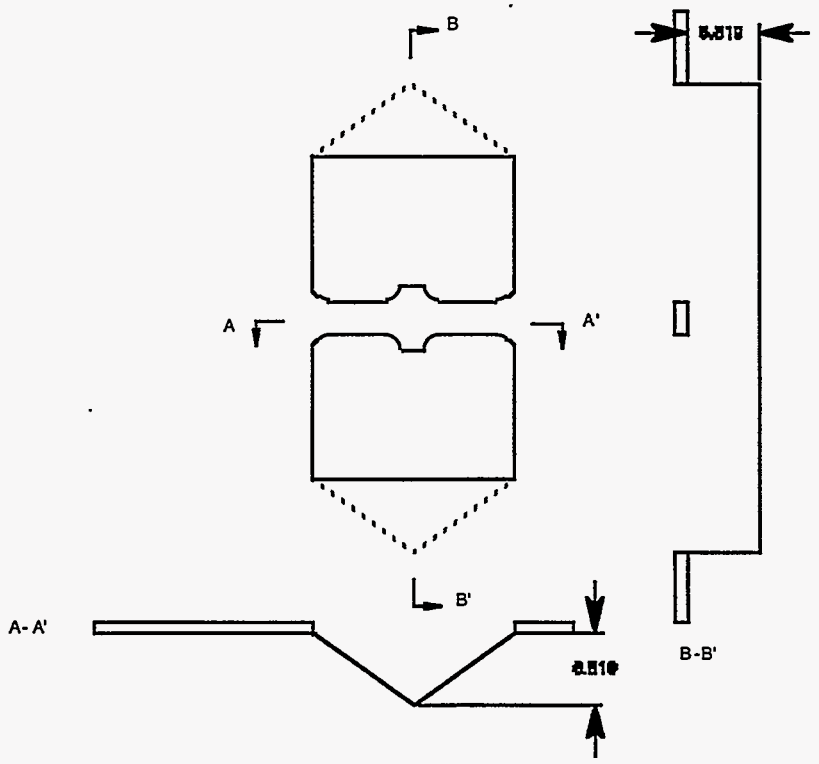

Figure 6. Schematic of a beam suspended over a pit etched in (110) silicon. Two major cross-sections of the pit are shown to illustrate the shape of the pit formed. The dotted lines again indicate the (111) surfaces formed. By referring back to an actual SEM micrograph, see Fig. 4, these aspects of the silicon etch can be related to the schematics of Figures 5 and 6.

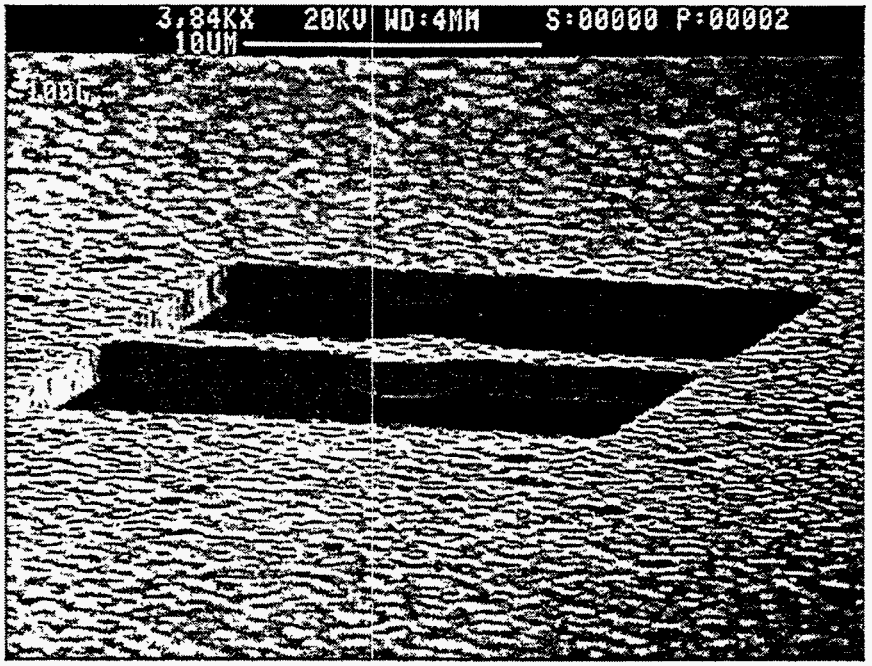

Figure 7a. Perspective SEM view of an aluminum beam suspended above a well etched in (110) silicon. The beam length is 20 microns, width 3 microns and thickness of 1.08 microns. The granular surface is due to the grain structure of the sputtered aluminum.

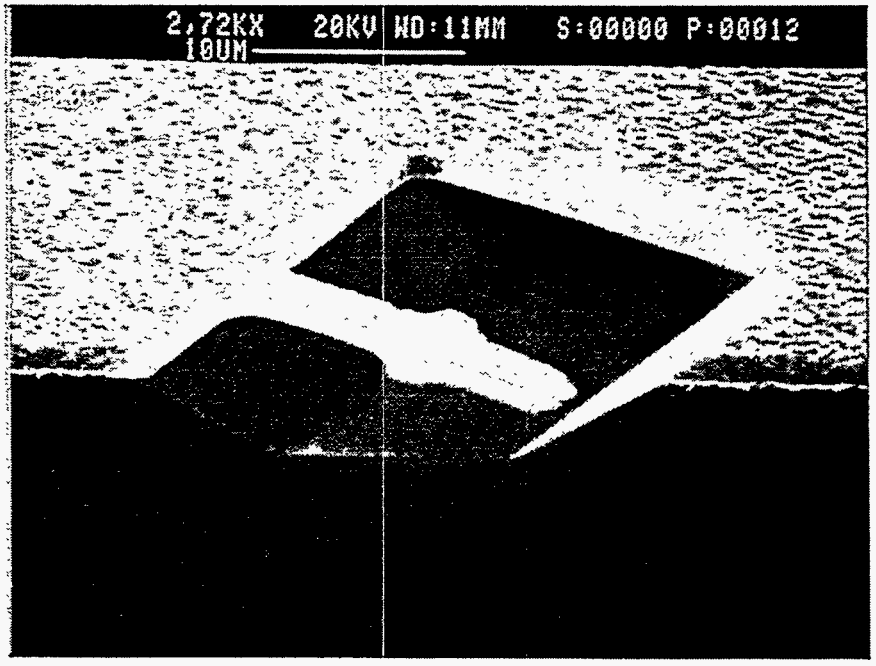

Figure 7b. Perspective SEM view of an aluminum beam like the one in figure 4a except that the wafer cleave for the SEM sample fractured this beam and well allowing a better view of the well surfaces and the beam cross-section. Note the lack of undercut at the remaining beam boundary and the undercut of the aluminum pattern at the upper end. These can be related to Figure 6.

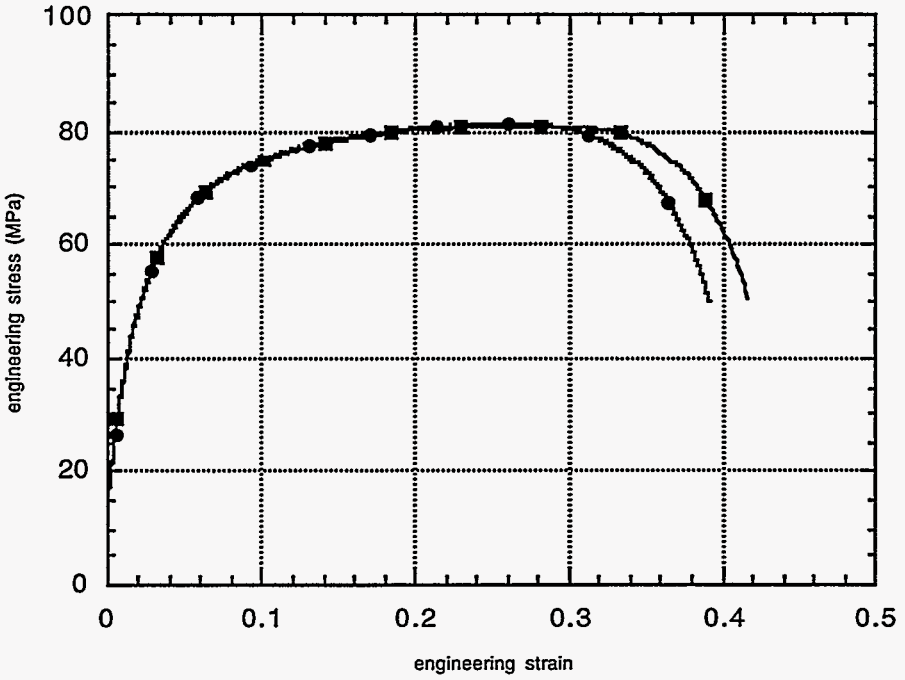

Figure 8. Engineering stress-strain response determined for 1100-0 aluminum plate.

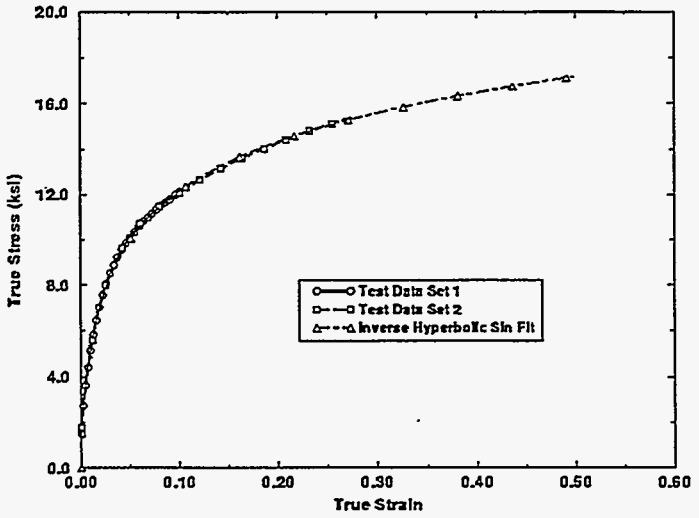

Figure 9. True stress-strain curve for 1100-0 aluminum and their inverse hyperbolic sin fit.

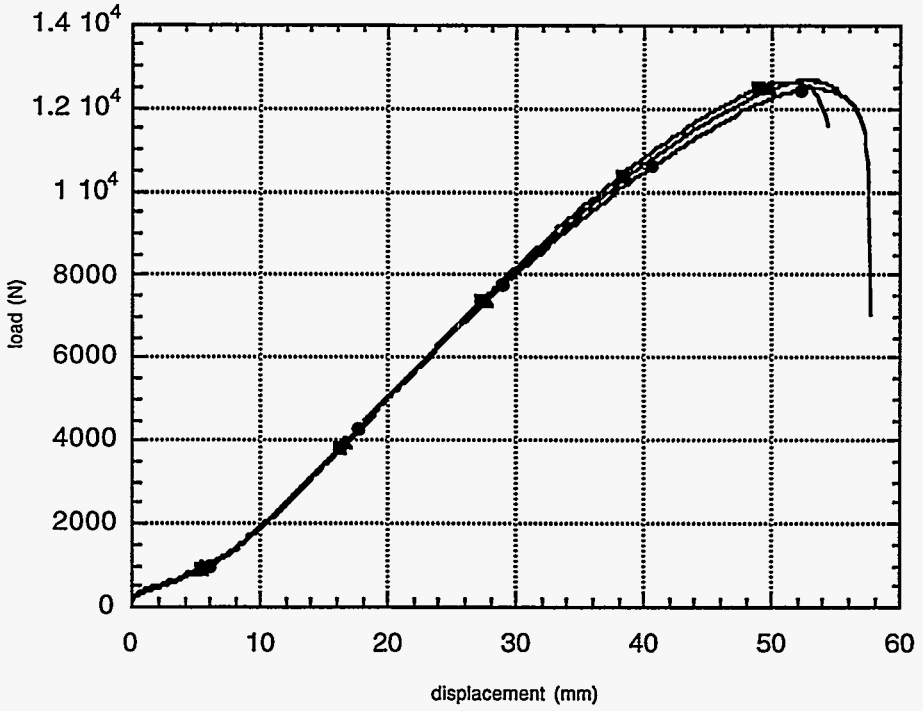

Figure 10. Force-displacement response of 1100-0 continuum-scale test structure.

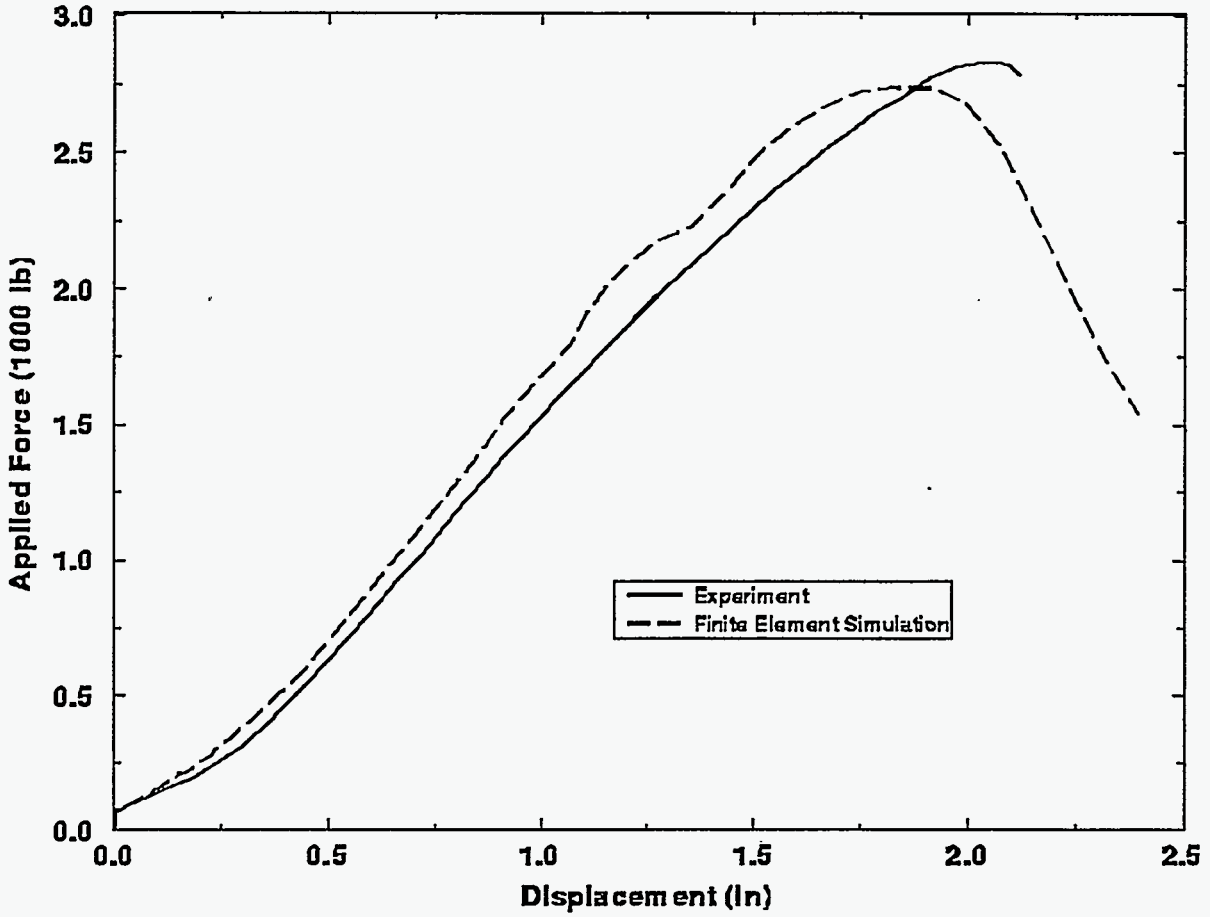

Figure 11. Force-displacement response predicted by finite element simulation of continuum-scale structure compare with experimental result.

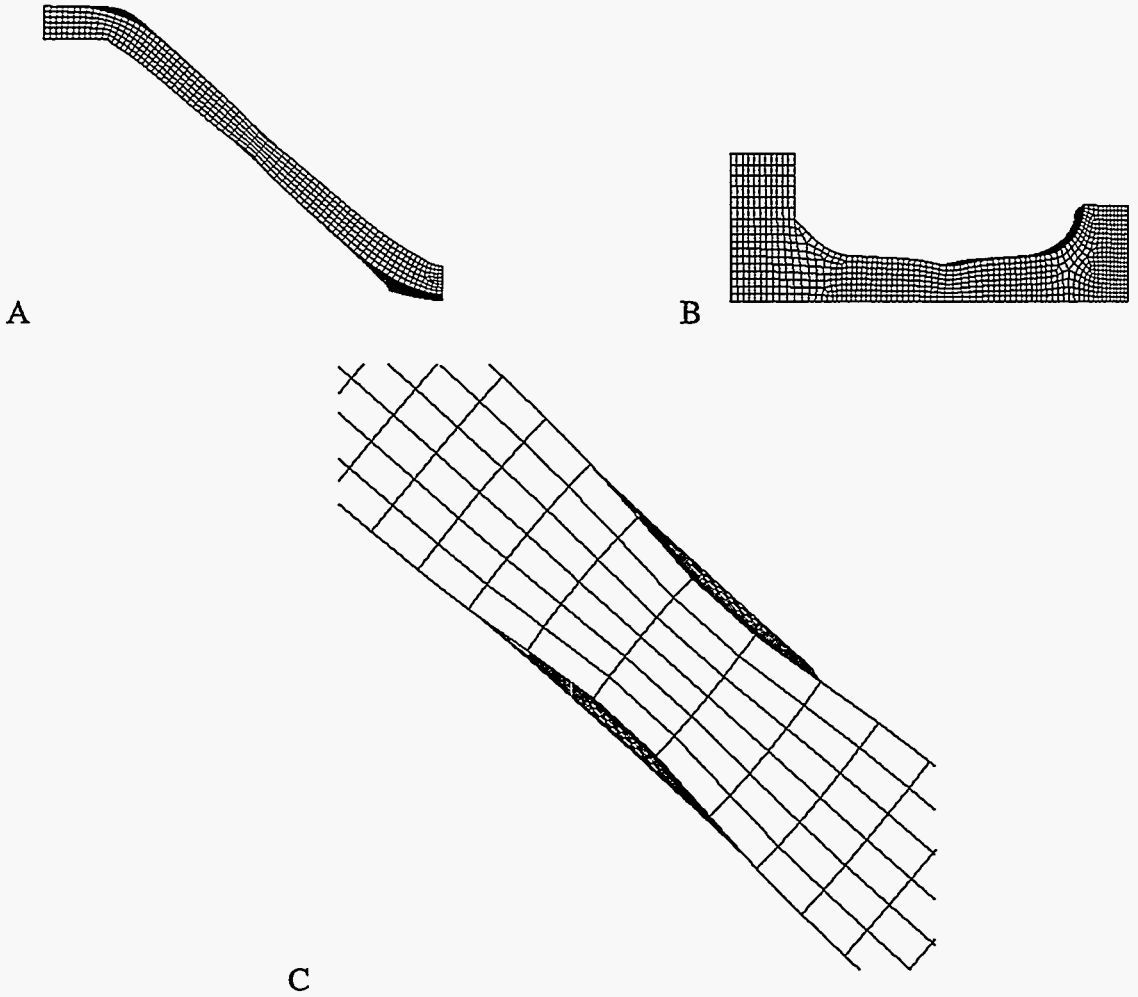

Figure 12. Details of the deformed geometry from a finite element simulation of the continuum-scale test structure.

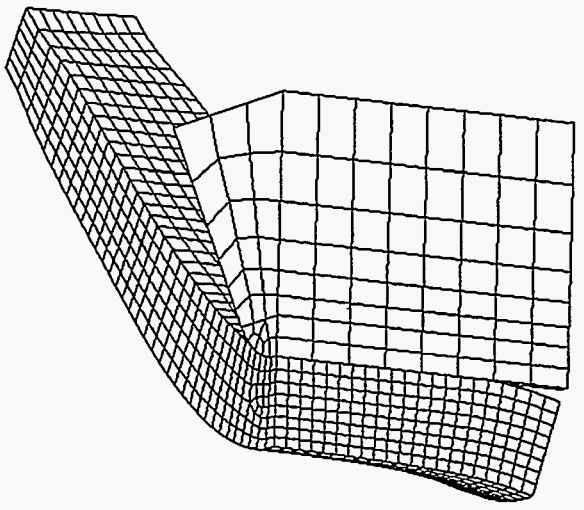

Figure 13. Detail of the deformed geometry from a finite element simulation of the continuum-scale test structure showing curvature of the contact pad away from the punch.

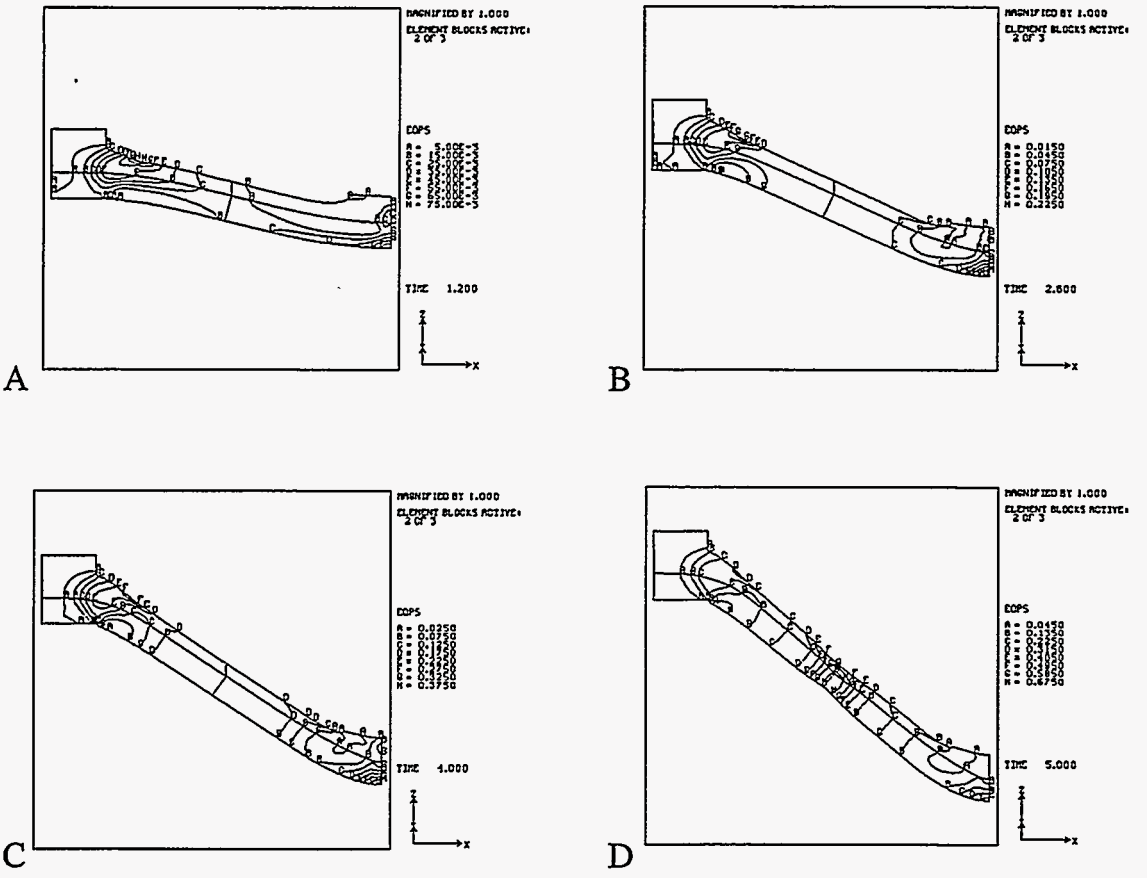

Figure 14. Computed plastic strain contours from finite element simulation of the continuum-scale test structure for deflections of (A) 0.5 in, (B) 1.0 in, (C) 1.5 in, (D) 2.0 in.

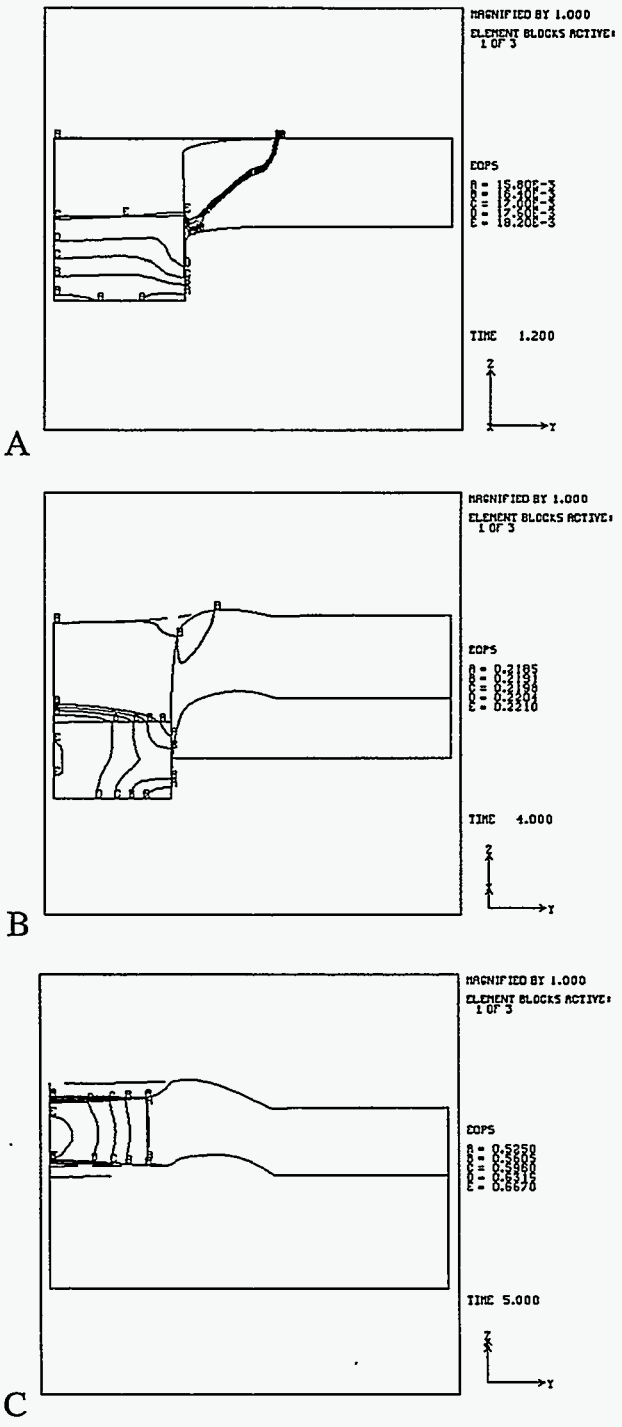

Figure 15. Computed plastic strain contours from finite element simulation of the continuum-scale test structure for deflections of (A) 0.5 in, (B) 1.6 in, (C) 2.0 in.

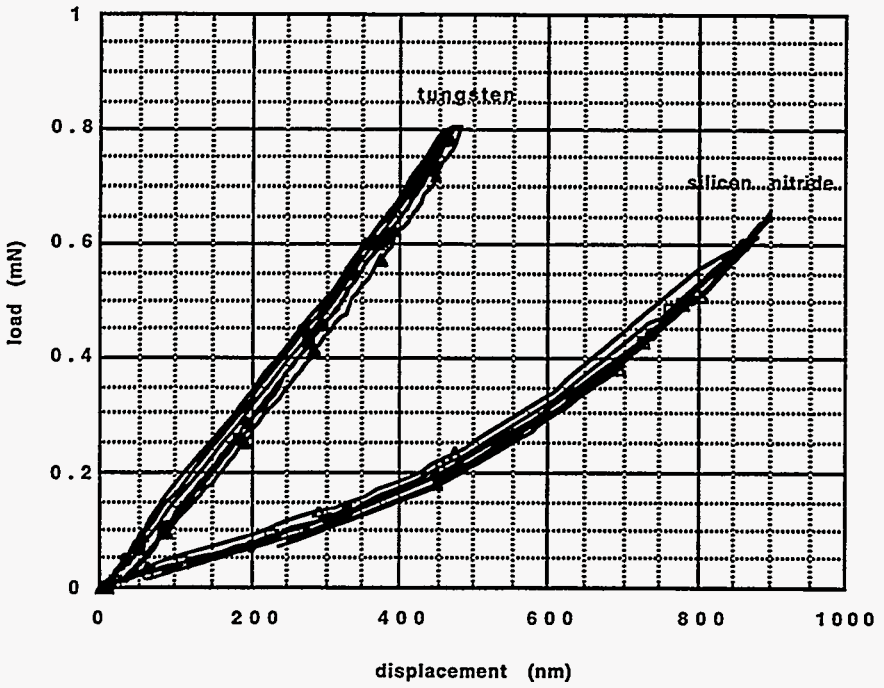

Figure 16. Force-displacement curves for micromechanical structures fabricated from tungsten and silicon nitride.

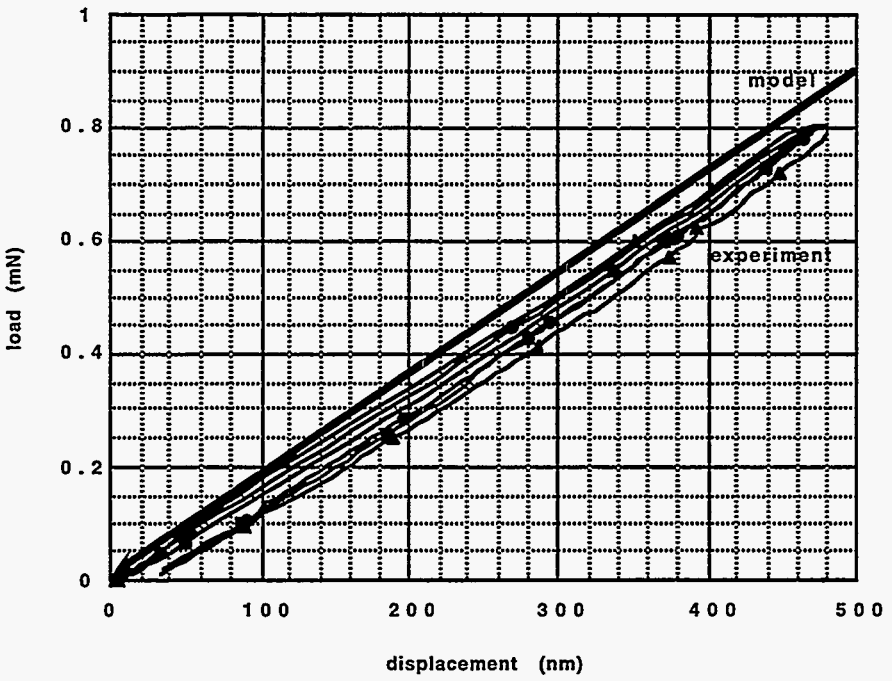

Figure 17. Force-displacement response curve calculated from small strain beam theory compared with experimental result for tungsten micromechanical test structures.

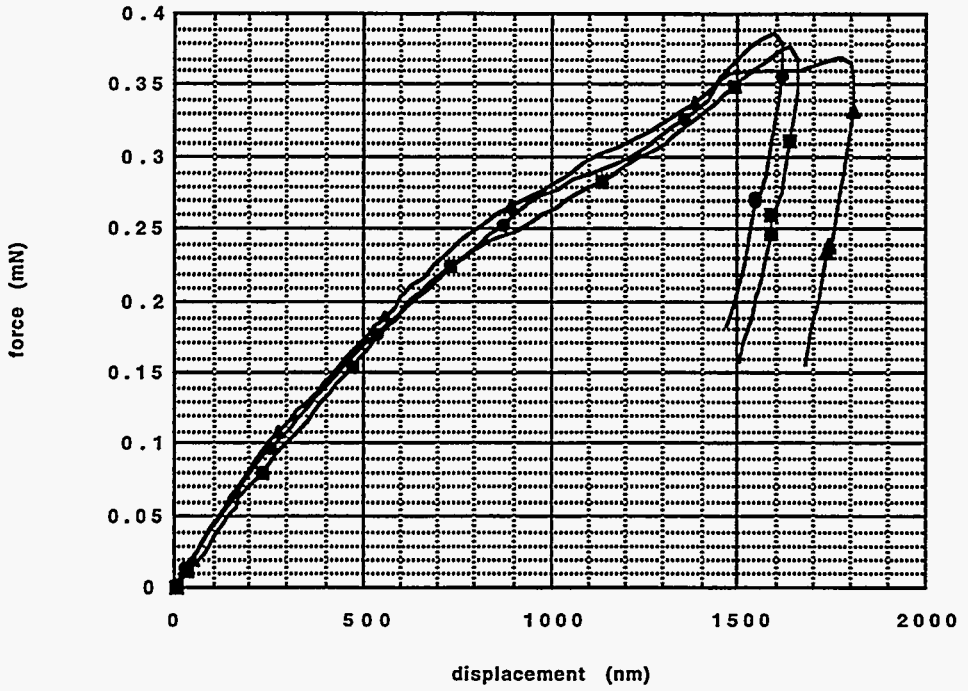

Figure 18. Force-displacement response curves for micromechanical test structures fabricated from aluminum .

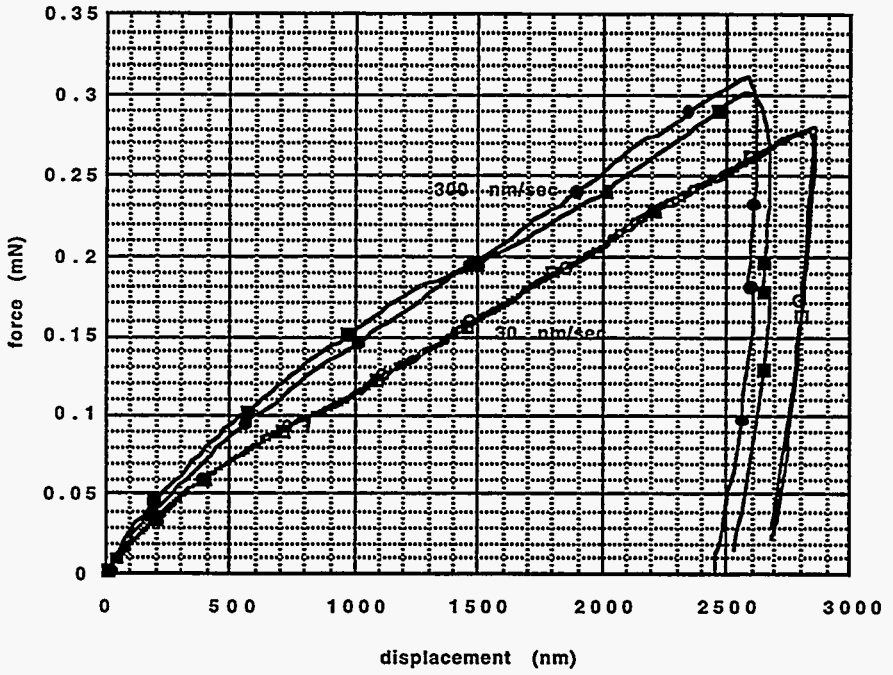

Figure 19. Force-displacement response curves for micromechanical test structures fabricated from aluminum and tested at different loading rates.

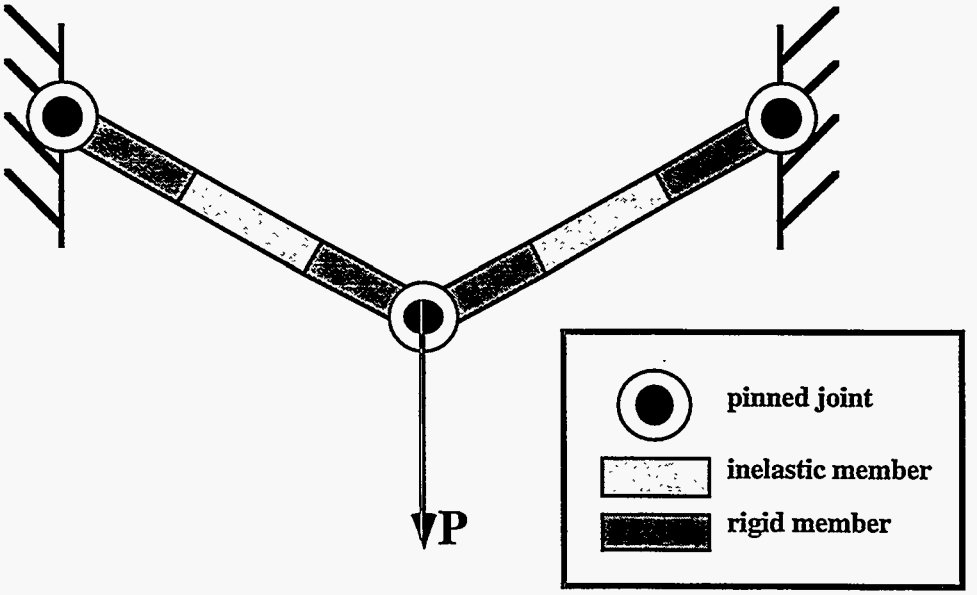

Figure 20. Schematic illustration of the mechanical model used to analyze the response of the micromechanical test structure.

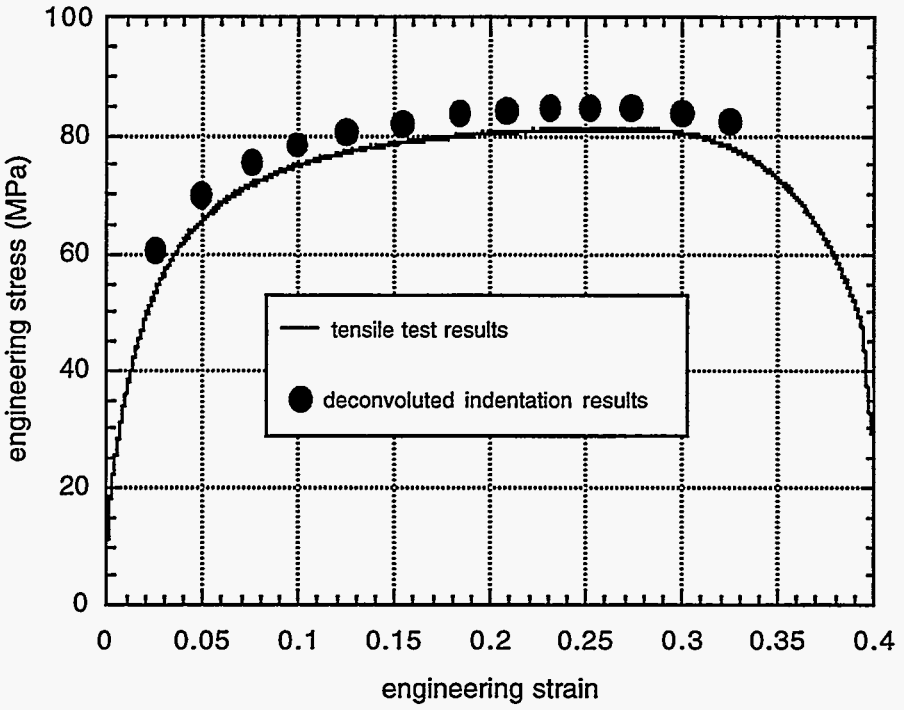

Figure 21. Comparison of deconvoluted macroscale test structure force-displacement data with experimental engineering stress-strain curve.

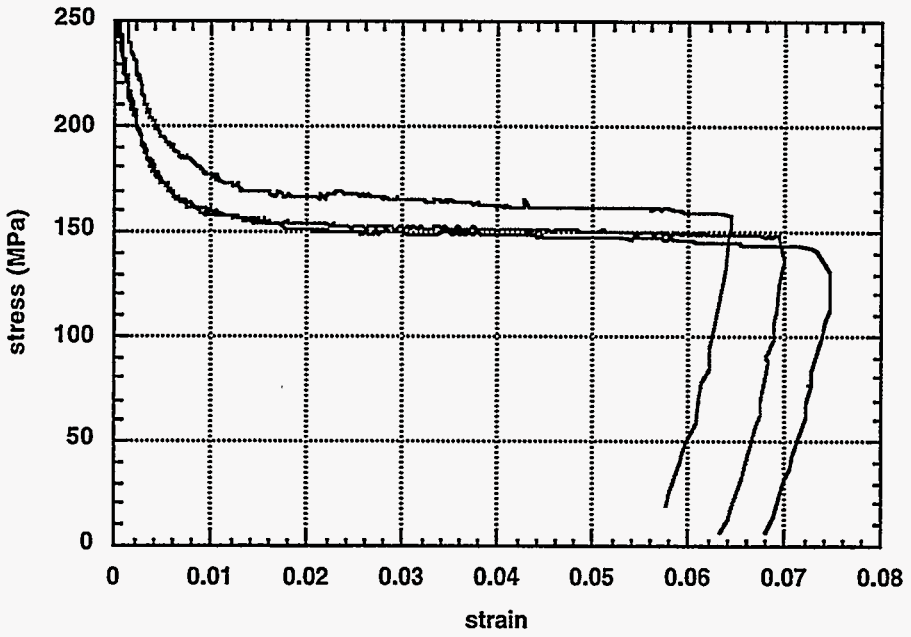

Figure 22. Deconvoluted force-displacement data for several aluminum microscale test structures.

Distribution:

1	MS	1079	A. D. Romig, Jr., 1300
1		0333	P. J. McWhorter, 1325
5		1080	J. J. Sniegowski, 1325
1		1435	H. J. Saxton, 1800
1		0342	R. J. Salzbrenner, 1805
1		0340	D. T. Schmale, 1831
1		0340	W. R. Cieslak, 1832
5		0333	R. J. Bourcier, 1841
1		0333	A. J. Hurd, 1841
1		0841	P. J. Hommert, 9100
1		0333	H. S. Morgan, 9117
5		0443	V. L. Porter, 9117
1		1436	LDRD Business Office, 4523
1		9018	Central Technical Files, 8523-2
5		0899	Technical Library, 4414
2		0619	Review & Approval Desk, 12630 For DOE/OSTI